Spin-Lattice Relaxation and the Calculation of Gain, Pump Power, and Noise Temperature in Ruby

J. R. Lyons
Telecommunications Systems Section

This article describes how a quantitative analysis of the dominant source of relaxation in ruby spin systems is used to make predictions of key maser amplifier parameters. The spin-lattice Hamiltonian which describes the interaction of the electron spins with the thermal vibrations of the surrounding lattice is obtained from the literature. Taking into account the vibrational anisotropy of ruby, Fermi's rule is used to calculate the spin transition rates between the maser energy levels. The spin population rate equations are solved for the spin transition relaxation times, and a comparison with previous calculations is made. Predictions of ruby gain, inversion ratio, and noise temperature as a function of physical temperature are made for 8.4-GHz and 32-GHz maser pumping schemes. The theory predicts that ruby oriented at 90 deg will have approximately 50 percent higher gain in dB and slightly lower noise temperature than a 54.7-deg ruby at 32 GHz (assuming pump saturation). A specific calculation relating pump power to inversion ratio is given for a single channel of the 32-GHz reflected wave maser.

I. Introduction

Ruby has been the active material employed in all DSN masers [1], and is again being considered for use at 32 GHz. In order to be able to predict the best operating point (i.e., crystal orientation, magnetic field intensity, and pumping scheme) available at a particular frequency and temperature, it is necessary to understand the relaxation behavior of the spins.

The spins in ruby are Cr^{3+} ions introduced as an impurity in the sapphire lattice. Because the spins are localized in the lattice, they obey classical particle statistics and have a Boltzmann distribution of energies at thermal equilibrium. To achieve maser operation, a spin population inversion is created by pumping the appropriate transitions at their resonance frequencies [2]. The incoming signal is then amplified by inducing stimulated emission between the signal transition levels. The amount of pump power required to maintain the population inversion depends on the rate at which the spins relax back to lower levels. With a knowledge of the relaxation rates, one may compute the corresponding inversion ratio, gain, and noise temperature of the ruby. Conduction losses would, of course, be accounted for separately.

The dominant spin relaxation mechanism in ruby at microwave frequencies and liquid He temperatures is due to interaction of the spins with the lattice, the so-called Kronig-Van Vleck mechanism [13]. Thermal vibrations of the Al_2O_3 lattice induce spin transitions via spin-orbit coupling. A so-called magneto-elastic tensor which characterizes the coupling of the Cr^{3+} ions to the lattice has been measured at 10 GHz [3]. Assuming the "direct" process of relaxation in which a single quantum of energy is exchanged between the spins and the lattice, Donoho [4] calculated the spin relaxation rates for an isolated spin based on the measured value of the magneto-elastic tensor. Based largely on Donoho's work, the calculation of relaxation rates was performed at 32 GHz for maser pumping schemes of interest.

As a means of comparing theory with experiment, Donoho also calculated the relaxation times associated with the saturation and recovery of a pair of spin levels. The calculation is performed by solving a linear set of first-order differential equations involving the level populations to determine the characteristic times associated with the return to equilibrium. The relaxation times depend on field strength, crystal orientation, and temperature, and are readily compared with measured values. Varying degrees of agreement between theory and experiment have been reported in the literature [5]. Because of the dependence of the measured relaxation times on crystal growth procedure, we are having measurements performed at the University of California, San Diego on Union Carbide ruby at frequencies of 9 GHz and 35 GHz. Note that the measurement of relaxation times is important not only in verifying the theory, but also because shorter relaxation times generally imply greater pump power requirements.

In addition to computing relaxation times, the present work computes the resulting spin populations for various amounts of pump power. Knowing the spin populations, all parameters of interest, such as ruby gain and noise temperature, may be determined. Hence, this theory provides a means of comparing in detail the different operating schemes for a 32-GHz maser at various temperatures. Experiments are being planned to measure inversion ratio, gain, and noise temperature or ruby at the 32-GHz operating points of interest.

It should be pointed out that a significant approximation has been made in assuming that the lattice interacts with an isolated spin. The Cr concentration is actually dilute (~ 0.05 percent), but if the ions cluster or if significant amounts of magnetic impurities or crystal imperfections are present, the relaxation behavior of the spins can be greatly modified [5]. In this work it is assumed that spin-spin interactions do not significantly affect the spin relaxation rates, but experiment may prove this to be a poor assumption.

This article proceeds as follows. Section II discusses the spin and spin-lattice Hamiltonians for ruby. Section III outlines the calculation of the spin-lattice transition rate. Section IV describes the solution of the time-dependent rate equations for the relaxation times and compares them with Donoho's [4] results. Section V discusses the calculation of inversion ratio, gain, pump power, and noise temperature. Conclusions are presented in Section VI.

II. Spin and Spin-Lattice Hamiltonians

A. Spin Hamiltonian

The spin Hamiltonian formalism [6, 13] is a semiempirical technique for describing the interaction of the electron spin of a paramagnetic ion with the static crystal electric field and applied magnetic field. Evaluation of the spin Hamiltonian yields values for the spin energy levels and rates of spin transition between levels due to the application of an RF magnetic field. The spin-lattice Hamiltonian is also a semiempirical formalism, but it describes the interaction of the paramagnetic ion spin with the time-varying crystal electric field associated with thermal lattice vibrations.

The spin Hamiltonian for ruby is discussed in [8], but a brief review is given below for completeness. The spin Hamiltonians for several other potential maser materials have been evaluated recently [9].

The form of the spin Hamiltonian often reflects the symmetry of the surrounding crystal field. In ruby, Cr^{3+} ions enter the Al_2O_3 lattice substitutionally for Al^{3+}. Each Al/Cr ion is surrounded by a distorted octahedron of O^{2-} ions such that the local site symmetry is C_3. The trigonal axis of the site, which coincides with the c axis of the ruby, is labeled the z axis, as shown in Fig. 1. The spin Hamiltonian for ruby is [10]

$$H_s = g\beta\overline{B}\cdot\overline{S} + D\left(S_z^2 - \frac{5}{4}\right) \tag{1}$$

where the spectroscopic splitting factor is approximately isotropic with the value $g = 1.98$, β is the Bohr magneton, $\overline{B}$ is the applied dc magnetic field, and the crystal field splitting factor is $D = -5.73$ GHz. S_z is the z component of the vector or spin operators,

$$\overline{S} = S_x\hat{x} + S_y\hat{y} + S_z\hat{z} \tag{2}$$

where the S_i are given in standard texts on quantum mechanics [11].

The first term in Eq. (1) is the Zeeman interaction and the second term represents the interaction of the spin with the static crystal electric field via spin-orbit coupling. Because the ground-state orbital is a singlet, the orbital angular momentum is quenched [13]. Hence, the crystal field splitting may be said to arise from admixture of the spin with the orbital angular momentum of higher-lying orbitals. Applying second-order perturbation theory, one obtains a splitting term that is second order in spin, as shown by Eq. (1). Detailed accounts of the derivation of the form of Eq. (1) based on the equivalent operator method are given elsewhere [8]. The parameter D is determined empirically, as a first-principles calculation is very difficult, perhaps because the bonding is partly ionic and partly covalent.

Cr is a transition metal element with the electronic configuration $3d^54^1_s$. The Cr^{3+} ion has the configuration $3d^3$. For the free ion, $L = 3$ and $S = 3/2$, so the term is ${}^4F_{3/2}$. A qualitative and simplified energy splitting diagram for Cr in sapphire showing the sequence of degeneracy removing perturbations is given in Fig. 2 [13].

To determine the spin energy levels, each spin state is expressed as a sum of pure spin states, that is, quantum states in which spin-orbit coupling is neglected, as follows:

$$\left|\Psi_i\right\rangle = a_i\left|+\frac{3}{2}\right\rangle + b_i\left|+\frac{1}{2}\right\rangle + c_i\left|-\frac{1}{2}\right\rangle + d_i\left|-\frac{3}{2}\right\rangle \tag{3}$$

The eigenvalue equation

$$H_s \mid \Psi_i\rangle = E_i \mid \Psi_i \tag{4}$$

is solved for the energies E_i and eigenvectors, $|\Psi_i\rangle$. Knowing the eigenstates, one may calculate W_{ij}, the rate of spin transitions stimulated by the time-varying magnetic field $\overline{H}_1$ between levels i and j, from Fermi's rule [2]:

$$W_{ij} = \frac{1}{4}\gamma^2 g_{ij}(f)| < \Psi_i|\overline{H}_1^* \cdot \overline{S}|\Psi_j > |^2 \tag{5}$$

where $\gamma = g\beta\mu_0/\hbar$ and $g_{ij}(f)$ is the line shape function as a function of frequency. Plots of energy levels versus B and isofrequency plots of B versus θ for ruby are given by Schultz-duBois [10].

An important point concerning the mixing of pure spin states should be made. For pure spin states, the selection rule $\Delta M = \pm 1$ applies, where M is the spin quantum number equal to 3/2, 1/2, −1/2, or −3/2 for $S = 3/2$. When spin-orbit interactions are included for a Cr^{3+} ion in a crystal, the resulting spin quantum states are a mixture of pure spin states, and as such cannot be labeled by a single value of M. Therefore, the $\Delta M = \pm 1$ rule cannot be strictly applied. This mixing of pure spin states is essential to continuous wave (CW) maser operation.

B. Spin-Lattice Hamiltonian

So far, the time-varying crystal field arising from lattice vibrations has been neglected. To describe the effect lattice vibrations have on the spin states, it is convenient to define a spin-lattice Hamiltonian, H_{SL} (derivations of the spin-lattice Hamiltonian are given in [14, 15]. Since the lattice vibrations may cause a slightly anisotropic perturbation of the crystal field, a reasonable form for H_{SL} is [4]

$$H_{SL} = \sum_{ij} d_{ij}S_iS_j, \quad i,j = x,y,z \tag{6}$$

where $|d_{ij}| \ll |D|$. For the one-phonon (direct) process of energy exchange, Van Vleck [16] assumed that H_{SL} was linear in strain. The d tensor may then be expressed as

$$d_{ij} = \sum_{kl} G_{ijkl}e_{kl}, \quad k,l = x,y,z \tag{7}$$

where G is a fourth-rank tensor having many of the symmetry properties of the classical elastic stiffness tensor relating stress and strain in a material. The tensor e is the classical strain given by

$$e_{kl} = \frac{1}{2}\left(\frac{\partial u_k}{\partial x_l} + \frac{\partial u_l}{\partial x_k}\right) \tag{8}$$

where u_k is the displacement of atoms in the direction x_k. The above form of H_{SL} neglects spin-spin interactions.

Calculation of the magneto-elastic-tensor G is of the same order of difficulty as calculation of the spin Hamiltonian parameter D. Therefore, G is determined experimentally. In [3] G was measured by applying a known uniaxial stress to a ruby crystal and observing the change in the EPR spectrum. The spin-lattice Hamiltonian given by Eqs. (6) and (7) is treated as a static perturbation to the energy levels computed from the spin Hamiltonian. The measurements were performed at 10.1 GHz at room temperature. Line shifts were in the range of 10 to 50 Gauss when the crystals were strained. Five crystal samples were employed, each having a different stress axis. The components of G were obtained by least-squares analysis of the data. The Cr concentration of the samples was thought to be ≈ 0.05 percent. At this concentration, spin-spin interactions may have a non-negligible effect on the spectra, so the G tensor values could be somewhat in error; however, this possibility has not been investigated.

The number of independent components in G can be reduced by symmetry arguments. The form of a fourth-rank tensor with C_3 symmetry is given in [17], and is shown to have twelve independent components. Choosing trace $(H_{SL}) = 0$, which shifts the corresponding energy levels by an insignificant constant, reduces the number of independent components to ten. The G tensor satisfies $G_{ijkl} = G_{jikl} = G_{ijlk}$, and so may be written in Voigt notation by defining the indices $1 = xx$, $2 = yy$, $3 = zz$, $4 = yz$, $5 = xz$, $6 = xy$. In Voigt notation G has the form

$$G = \begin{bmatrix} G_{11} & G_{12} & -G_{33}/2 & G_{14} & -G_{25} & G_{16} \\ G_{12} & G_{11} & -G_{33}/2 & -G_{14} & G_{25} & -G_{16} \\ -(G_{11}+G_{12}) & -(G_{11}+G_{12}) & G_{33} & 0 & 0 & 0 \\ G_{41} & -G_{41} & 0 & G_{44} & G_{45} & G_{52} \\ -G_{52} & G_{52} & 0 & -G_{45} & G_{44} & G_{41} \\ -G_{16} & G_{16} & 0 & G_{25} & G_{14} & \frac{1}{2}(G_{11}-G_{12}) \end{bmatrix} \qquad (9)$$

The G values (in GHz) used in [4] and in this work are the following:

$$\begin{array}{ll} G_{11} = 124.6 & G_{41} = -15.0 \\ G_{12} = -35.8 & G_{25} = 45.0 \\ G_{33} = 181.2 & G_{52} = 45.0 \\ G_{44} = 54.0 & G_{16} = 0 \\ G_{14} = -15.0 & G_{45} = 0 \end{array}$$

The factor of $\hbar^2$ from the $S_i S_j$ term is absorbed into the G values.

For interactions with the Al_2O_3 lattice, the Cr^{3+} ions can be considered to occupy two inequivalent sites, as discussed in [3]. These sites are related by a 2-fold rotation about the x axis. For the two sites all the elements of G have the same magnitude, but G_{25}, G_{52}, G_{16}, and G_{45} have opposite signs. In [4] and in this work only one Cr site, specified by the elements of G given above, is accounted for. Computer experiments have shown that the second site does not lead to significantly different relaxation times or inversion ratios.

The tensor G characterizes the effect a given strain has on the EPR spectrum. To relate G to the thermal lattice vibrations one must know the strain associated with a given lattice mode and also the number of phonons present (i.e., the phonon occupation number). Since the phonon wavelengths of interest are $\sim 10^{-4}$ cm (for a sound velocity $\sim 10^6$ cm/sec), the atoms may be assumed to undergo displacements of equal amplitude in any unit cell. (This is an approximation since the different mass ions would undergo slightly different displacements, thus modifying the local crystal field.) Then, for phonons of wavevector $\bar{k}$ and polarization vector $\hat{\epsilon}_p$, the displacement may be written as

$$\bar{u}(\bar{r}) = \left(\frac{\hbar}{2M\omega}\right)^{1/2} \left(a^{+}_{k,p} - a_{-k,p}\right) \hat{\epsilon}_p e^{i\bar{k}\cdot\bar{r}} \qquad (10)$$

where M is the crystal mass, ω is the angular frequency, and a and a^{+} are the phonon annihilation and creation operators. The phonon operators arise from an analogy with the quantum harmonic oscillator, as discussed in any solid state physics text [18]. They have the following properties:

$$a^+_{k,p} \left| n_{k,p} \right\rangle = \sqrt{n_{k,p}+1} \left| n_{k,p}+1 \right\rangle \tag{11}$$

$$a_{k,p} \left| n_{k,p} \right\rangle = \sqrt{n_{k,p}} \left| n_{k,p}-1 \right\rangle \tag{12}$$

where $n_{k,p}$ is the phonon occupation number for the state k, p, and where subscript k is the mode wavevector and p is the mode polarization (two transverse and one longitudinal). From Eqs. (8) and (10), the strain becomes

$$e_{ij} = \left(\frac{\hbar}{8M\omega}\right)^{1/2} \left(a^+_{k,p} - a_{-k,p}\right)\left(\epsilon_{p,i}k_j + \epsilon_{p,j}k_i\right) e^{i\bar{k}\cdot\bar{r}} \tag{13}$$

where $i, j = x, y, z$.

III. The Spin-Lattice Transition Rate

In determining the G tensor, the spin-lattice Hamiltonian is static since the applied strain is static. However, in modeling the interaction of the Cr spin with the thermal lattice vibrations, the strain is time periodic. The resulting H_{SL} is therefore a dynamical Hamiltonian requiring the application of time-dependent perturbation theory, specifically Fermi's rule.

We are interested in lattice modes that are on "speaking terms" with the spins, that is, vibrating at frequencies that correspond to spin transitions. Fermi's rule is used to calculate the transition probability rate, ω_{ij}, for spin transitions from level i to level j due to spin-lattice interaction. Since ruby is vibrationally anisotropic, an integration over all possible phonon directions is performed. The three phonon polarizations (one longitudinal and two transverse) and the phonon density of states are also accounted for. Applying Fermi's rule,

$$\omega_{ij} = \frac{2\pi}{\hbar^2} \int_{4\pi} \sum_{p=1}^{3} \left| \left\langle \Psi_i, n_{k,p} \,\middle|\, H_{SL} \,\middle|\, \Psi_j, n_{k,p}+1 \right\rangle \right|^2 \times \rho(\omega) \frac{d\Omega}{4\pi} \tag{14}$$

where $|\Psi_i\rangle$ is the state vector for level i as determined from Eq. (4), $|n_{k,p}\rangle$ is the nth phonon occupation state for a phonon with wavevector k and polarization p, $\rho(\omega) = \partial N/\partial\omega$ is the density of phonon states, as a function of frequency, and $d\Omega$ is an infinitesimal solid angle. In Eq. (14), the perturbing Hamiltonian H_{SL} changes the quantum state from that of a spin in state i and n phonons in state k, p to that of a spin in state j and $n+1$ phonons in state k, p. This corresponds to the creation of a phonon when a spin drops from a higher energy state to a lower energy state.

From [18], the density of states for each polarization in a periodic solid is

$$\rho(\omega) = V \frac{k^2}{2\pi^2} \frac{dk}{d\omega} \tag{15}$$

where V is the crystal volume. Making the Debye approximation in which the velocity of sound v is a constant for each polarization type, the dispersion relation is simply $\omega = vk$. Equation (15) then becomes

$$\rho(\omega) = \frac{V\omega^2}{2\pi^2 v^3} \tag{16}$$

The Debye temperature of sapphire is 980 K [19], which corresponds to a frequency of $\approx 2 \times 10^{13}$ Hz, so the Debye approximation is assumed to be valid for the one-phonon relaxation process. Anharmonic crystal interactions and multiple phonon processes are neglected.

Consider now the matrix element in Eq. (14). Substituting Eqs. (6) and (7) for H_{SL} in Eq. (14), and separating spin and phonon operators, one obtains

$$\begin{aligned} \left\langle \Psi_i, n_{k,p} \,\middle|\, H_{SL} \,\middle|\, \Psi_j, n_{k,p}+1 \right\rangle &= \left(\frac{\hbar}{8M\omega}\right)^{1/2} \\ &\times \left\langle n_{k,p} \,\middle|\, a^+_{k,p} - a_{-k,p} \,\middle|\, n_{k,p}+1 \right\rangle e^{i\bar{k}\bar{r}} \\ &\times \sum_{mnst} G_{mnst} \left\langle \Psi_i \,\middle|\, S_m S_n \,\middle|\, \Psi_j \right\rangle \left(\epsilon_{p,s}k_t + \epsilon_{p,t}k_s\right) \end{aligned} \tag{17}$$

where $m, n, s, t = x, y, z$. Applying Eqs. (11) and (12), the phonon matrix element becomes

$$\left\langle n_{k,p} \,\middle|\, a^+_{k,p} - a_{-k,p} \,\middle|\, n_{k,p}+1 \right\rangle = -\sqrt{n_{k,p}+1} \tag{18}$$

For a large number of spins, $n_{k,p}$ may be replaced by the average phonon occupation number as given by a Bose-Einstein distribution of phonons (spin-one quasi-particles) at the lattice temperature T,

$$(n_{k,p})_{avg} = \frac{1}{e^{\frac{\hbar\omega}{kT}} - 1} \tag{19}$$

Substituting Eqs. (16) through (19) into Eq. (14), one obtains

$$\omega_{ij} = \frac{\omega}{32\pi^2 \rho_c \hbar} \frac{1}{1 - e^{\frac{-\hbar\omega}{kT}}} \int_{4\pi} \sum_{p=1}^{3} \times \left\{ \left| \sum_{mnst} G_{mnst} \Big\langle i \Big| S_m S_n \Big| j \Big\rangle \times (\epsilon_{p,s} k_t + \epsilon_{p,t} k_s) \right|^2 \frac{1}{v_{k,p}^3} \right\} d\Omega \tag{20}$$

where Ψ_i and Ψ_j have been denoted by i and j, ρ_c is the crystal density, and $v_{k,p}$ is the phonon velocity for mode k,p. Equation (20) is Eq. (11) in [4].

In order to simplify Eq. (20), it is convenient to use Voigt notation and to make some new variable definitions. Define the direction cosines of the wavevector k as follows:

$$l_i = \frac{k_i}{k}, \quad i = x, y, z \tag{21}$$

Writing G in Voigt notation, the summation over m, n, s, t in Eq. (20) may be written as

$$\sum_{mnst} G_{mnst} \Big\langle i \Big| S_m S_n \Big| j \Big\rangle (\epsilon_{p,s} k_t + \epsilon_{p,t} k_s) = k \sum_{u,v=1}^{6} G_{uv} \Big\langle i \Big| S_u^2 \Big| j \Big\rangle L_{p,v} \tag{22}$$

where S_u^2 and $L_{p,v}$ are defined as follows:

$$\begin{aligned} S_1^2 &= S_x S_x & S_2^2 &= S_y S_y \\ S_3^2 &= S_z S_z & S_4^2 &= S_y S_z + S_z S_y \\ S_5^2 &= S_z S_x + S_x S_z & S_6^2 &= S_x S_y + S_y S_x \end{aligned} \tag{23}$$

and

$$\begin{aligned} L_{p,1} &= 2\epsilon_{p,x} l_x & L_{p,2} &= 2\epsilon_{p,y} l_y \\ L_{p,3} &= 2\epsilon_{p,z} l_z & L_{p,4} &= 2(\epsilon_{p,y} l_z + \epsilon_{p,z} l_y) \\ L_{p,5} &= 2(\epsilon_{p,z} l_x + \epsilon_{p,x} l_z) & L_{p,6} &= 2(\epsilon_{p,x} l_y + \epsilon_{p,y} l_x) \end{aligned} \tag{24}$$

Using the dispersion relation $\omega = 2\pi f = k v_{k,p}$, where f is the frequency of the spin transition between levels i and j, and substituting Eqs. (21) through (24) into Eq. (20) yields

$$\omega_{ij} = \frac{\pi^2}{2\rho_c h} \frac{f^3}{1 - e^{\frac{-hf}{kT}}} \int_{4\pi} \sum_{p=1}^{3} \times \left| \sum_{u,v=1}^{6} G_{uv} \langle i \mid S_u^2 \mid j \rangle L_{p,v} \right|^2 \frac{1}{v_{k,p}^5} \, d\Omega \tag{25}$$

Defining

$$A_{p,u} = \sum_{v=1}^{6} G_{uv} L_{p,v} \tag{26}$$

the modulus-squared quantity in Eq. (25) can be written as

$$\left| \sum_{u,v=1}^{6} G_{uv} \Big\langle i \Big| S_u^2 \Big| j \Big\rangle L_{p,v} \right|^2 = \sum_{q,r=1}^{6} A_{p,q} A_{p,r} \Big\langle i \Big| S_q^2 \Big| j \Big\rangle \Big\langle i \Big| S_q^2 \Big| j \Big\rangle^* \tag{27}$$

Substituting Eq. (27) into Eq. (25) and interchanging the integral and the sum over polarization with the sum over q and r, Eq. (25) becomes

$$\omega_{ij} = \frac{\pi^2}{2\rho_c h} \frac{f^3}{1 - e^{\frac{-hf}{kT}}} \sum_{q,r=1}^{6} B_{qr} \left\langle i \,\middle|\, S_q^2 \,\middle|\, j \right\rangle \left\langle i \,\middle|\, S_r^2 \,\middle|\, j \right\rangle^* \tag{28}$$

where

$$B_{qr} = \int_{4\pi} \sum_{p=1}^{3} A_{p,q} A_{p,r} \frac{1}{v_{k,p}^5} \, d\Omega \tag{29}$$

Equation (29) is evaluated by a numerical integration over 4π steradians. Specifically,

$$\int_{4\pi} \{ \ \} d\Omega = \int_0^{2\pi} \int_0^{\pi} \{ \ \} \sin\theta \, d\theta \, d\phi \tag{30}$$

where the double integral is evaluated as a double sum. Numerical experimentation shows that the double sum converges for a summation step of $\Delta\theta = \Delta\phi = 5$ deg.

The density of sapphire is 4.0 gm/cm^3 [20]. For G and f specified in units of GHz, $v_{k,p}$ in units of 10^5 cm/sec, and S_q^2 dimensionless, the constant in front of Eq. (28) becomes 8.2×10^{-7} and ω_{ij} has the units of sec^{-1}.

In order to evaluate Eqs. (24) and (29), one needs the phonon velocity and polarization vector for the three phonon polarizations for each wavevector direction in the 4π steradians. These are the quantities of interest in the so-called Christoffel equations [21], which describe elastic wave propagation in an anisotropic elastic medium. The equations are a coupled set of three equations of motion for volume elements of the crystal; Kittel [18] discusses the case of cubic symmetry.

Wachtman et al. [22] gives the appropriate equations for single-crystal Al_2O_3, which has trigonal symmetry. The elastic constants, c_{ij}, (Voigt notation) are defined by

$$\sigma_i = \sum_{j=1}^{6} c_{ij} \epsilon_j \tag{31}$$

where σ is the stress tensor and ϵ is the strain tensor. Values for the six independent elements of c_{ij} are determined at room temperature by a resonance method discussed in [22].

For the coordinate system of Fig. 1, the equations of motion for an elastic wave with frequency $\omega = \boldsymbol{k} \cdot v$ may be written as

$$\begin{bmatrix} A & H & G \\ H & B & F \\ G & F & C \end{bmatrix} \begin{bmatrix} \Delta x \\ \Delta y \\ \Delta z \end{bmatrix} = \rho_c v^2 \begin{bmatrix} \Delta x \\ \Delta y \\ \Delta z \end{bmatrix} \tag{32}$$

where Δx, Δy, Δz are the material displacements which taken together specify the polarization vector. The matrix elements A, B, C and F, G, H are functions of the c_{ij} and the wavevector direction cosines:

$$\begin{aligned} A &= c_{11} l^2 + \tfrac{1}{2}(c_{11} - c_{12}) m^2 + c_{44} n^2 + 2 c_{14} mn \\ B &= \tfrac{1}{2}(c_{11} - c_{12}) l^2 + c_{11} m^2 + c_{44} n^2 - 2 c_{14} mn \\ C &= c_{44}(l^2 + m^2) + c_{33} n^2 \\ F &= c_{14}(l^2 - m^2) + (c_{13} + c_{44}) mn \\ G &= 2 c_{14} lm + (c_{13} + c_{44}) ln \\ H &= \tfrac{1}{2}(c_{11} + c_{12}) lm + 2 c_{14} ln \end{aligned} \tag{33}$$

where $l = \sin\theta\cos\phi$, $m = \sin\theta\sin\phi$, and $n = \cos\theta$. For each wavevector direction in Eq. (30), Eq. (32) is solved for the phonon velocity and polarization, as given by the eigenvalues and eigenvectors, respectively, of the matrix in Eq. (32).

The B_{qr} quantities defined in Eq. (29) need only be calculated once for each Cr site; the resulting values are stored in computer memory. For Cr site number 1 (i.e., for G given by Eq. 9) the matrix B has the form

$$B = \begin{bmatrix} B_{11} & B_{12} & B_{13} & B_{14} & B_{15} & B_{16} \\ B_{12} & B_{11} & B_{13} & -B_{14} & -B_{15} & -B_{16} \\ B_{13} & B_{13} & B_{33} & 0 & 0 & 0 \\ B_{14} & -B_{14} & 0 & B_{44} & 0 & -B_{15} \\ B_{15} & -B_{15} & 0 & 0 & B_{44} & B_{14} \\ B_{16} & -B_{16} & 0 & -B_{15} & B_{14} & B_{66} \end{bmatrix} \tag{34}$$

where the independent components have the following values:

$$\begin{array}{ll} B_{11} = 32.2 & B_{16} = -0.0030 \\ B_{12} = -13.9 & B_{33} = 36.6 \\ B_{13} = -18.3 & B_{44} = 11.7 \\ B_{14} = -3.67 & B_{66} = 23.1 \\ B_{15} = -14.04 & \end{array} \tag{35}$$

For Cr site number 2 the B_{qr} have the same magnitude, but B_{15} and B_{16} have opposite signs. For the B_{qr} given above, ω_{ij} is calculated from Eq. (28) for each field intensity, angle, transition, and temperature of interest.

Finally, consider the frequency and temperature dependence of ω_{ij}. From Eq. (28), the temperature dependence is determined by the factor $(1 - e^{-hf/kT})^{-1}$, for which

$$\left(1 - e^{\frac{-hf}{kt}}\right)^{-1} \approx \begin{cases} \frac{kT}{hf}, & \frac{hf}{kT} \ll 1 \\ 1, & \frac{hf}{kT} \gg 1 \end{cases} \tag{36}$$

Thus, for $hf/kT \ll 1$, ω_{ij} is proportional to temperature, or, since the relaxation time T_1 is $\sim \omega_{ij}^{-1}$, $T_1 \sim T^{-1}$. A relaxation time inversely proportional to physical temperature is a characteristic of the one-phonon relaxation process, and has been observed for many paramagnetic materials (including ruby) at liquid He temperatures [13]. The multiple-phonon relaxation processes exhibit relaxation times with significantly different dependence on temperature, e.g., $T_1 \propto T^{-7}$ (Raman process).

The frequency dependence of ω_{ij} is contained in the factor $f^3 \cdot (1 - e^{-hf/kT})^{-1}$ and also in the mixing of spin states.

Also note the strong dependence of ω_{ij} on the velocity of sound. From Eqs. (28) and (29), $\omega_{ij} \sim v^{-5}$, so if long relaxation times are desired, a hard material such as sapphire is beneficial.

IV. Spin-Lattice Relaxation Times

The spin-lattice relaxation times, T_1, are of interest primarily because they are more accessible to measurement than the transition probability rates. The relaxation times are calculated by solving a set of time-dependent rate equations for the spin populations. The rate equations, not including pump-induced transition rates, for the ith level are [2, 4]

$$\frac{dn_i(t)}{dt} = \sum_{j=1}^{4}\Big(\omega_{ji}n_j(t) - \omega_{ij}n_i(t)\Big), \quad i = 1, \ldots, 4 \tag{37}$$

where $n_i(t)$ is the instantaneous spin population of level i. Conservation of the number of spins requires that

$$n_1 + n_2 + n_3 + n_4 = N \tag{38}$$

where N, the total number of spins, is constant. Equations (37) and (38) reduce to a system of three equations,

$$\dot{\bar{n}} = A\bar{n} + \bar{b} \tag{39}$$

where

$$\bar{n} = \begin{bmatrix} n_1 \\ n_2 \\ n_3 \end{bmatrix} \tag{40}$$

$$\bar{b} = \begin{bmatrix} \omega_{41} \cdot N \\ \omega_{42} \cdot N \\ \omega_{43} \cdot N \end{bmatrix} \tag{41}$$

and

$$A = \begin{bmatrix} A_{11} & \omega_{21} - \omega_{41} & \omega_{31} - \omega_{41} \\ \omega_{12} - \omega_{42} & A_{22} & \omega_{32} - \omega_{42} \\ \omega_{13} - \omega_{43} & \omega_{23} - \omega_{43} & A_{33} \end{bmatrix} \tag{42}$$

where

$$\begin{aligned} A_{11} &= -\left(\omega_{12} + \omega_{13} + \omega_{14} + \omega_{41}\right) \\ A_{22} &= -\left(\omega_{21} + \omega_{23} + \omega_{24} + \omega_{42}\right) \\ A_{33} &= -\left(\omega_{31} + \omega_{32} + \omega_{34} + \omega_{43}\right) \end{aligned} \tag{43}$$

Note that

$$\omega_{ji} = e^{\frac{-hf}{kT}} \omega_{ij} \tag{44}$$

where $f = f_i - f_j$, as can be shown by manipulation of Eq. (28).

Experimentally, the usual procedure for measuring T_1 is to saturate a pair of levels with a strong microwave pulse and observe the recovery of the same or another pair of levels as the spins return to thermal equilibrium. For noninteracting spins (i.e., no cross-relaxation) the recovery is exponential, with T_1 being identified as the time constant of the decay. A theoretical T_1 is determined by solving Eq. (39) for an appropriate set of initial conditions. For example, if levels one and two are saturated, then the initial conditions would be

$$\bar{n}(t=0) = \begin{bmatrix} \frac{1}{2}(N_1 + N_2) \\ \frac{1}{2}(N_1 + N_2) \\ N_3 \end{bmatrix} \tag{45}$$

where N_i is the thermal equilibrium spin population of level i. The N_i satisfy a Boltzmann distribution,

$$\frac{N_i}{N_j} = e^{\frac{-hf}{kT}} \tag{46}$$

and also satisfy the conservation relation,

$$N_1 + N_2 + N_3 + N_4 = N \tag{47}$$

The solution to Eq. (39) is straightforward and may be found in [23]:

$$\bar{n}(t) = \alpha_1 \bar{c}_1 e^{\lambda_1 t} + \alpha_2 \bar{c}_2 e^{\lambda_2 t} + \alpha_3 \bar{c}_3 e^{\lambda_3 t} - A^{-1}\bar{b} \tag{48}$$

where

$$\begin{bmatrix} \alpha_1 \\ \alpha_2 \\ \alpha_3 \end{bmatrix} = (\bar{c}_1\ \bar{c}_2\ \bar{c}_3)^{-1} \cdot \left(\bar{n}(0) + A^{-1}\bar{b}\right) \tag{49}$$

and the $\bar{c}_i$ are the eigenvectors of A (written as column vectors) with the corresponding eigenvalues λ_i. The normalized population difference between levels i and j is

$$\frac{n_i - n_j}{N_i - N_j} = 1 + A_1 e^{-t/T_1} + A_2 e^{-t/T_2} + A_3 e^{-t/T_3} \tag{50}$$

where the $T_i = -1/\lambda_i$ are the relaxation times, and the A_i are determined from the α_i and $\bar{c}_i$. Thus, the recovery of each pair of levels is characterized by three relaxation times. In fact, the same three relaxation times characterize the recovery between any pair of levels for a given initial condition; however, the amplitudes, A_i, will vary for the different transitions.

Donoho [4] plots T_i and A_i as a function of θ and transition for a frequency $f = 9.3$ GHz and a physical temperature $T = 4.2$ K. In [4] there are also several plots of T_1 versus frequency (1–10 GHz) for particular angles and transitions. Generally it was found that only one or two relaxation times were important, usually the longest two. These calculations were repeated as a check on the computer code. Table 1 compares two sets of T_i and A_i values from [4] with the author's calculations for an angle $\theta = 54.7$ deg. The T_i from the author's calculations are approximately a factor of one-half less than Donoho's results, which leads to better agreement between theory and experiment at 10 GHz [5, 24]. More troublesome, however, is the lack of consistent agreement among the A_i values. Although the cause of the disagreement is unknown, the disagreement is not considered significant in light of the consistent relaxation times computed.

Previous comparisons of experimental and theoretical values of T_1 have generally not shown good agreement even for very dilute ruby (~ 0.01 percent) [5]. For example, the relaxation times may be several times shorter than the theory predicts and may not have the angular dependence displayed by Donoho's results. However, Standley and Vaughan [24] made measurements on ruby grown by the so-called vapor phase modification to the flame-fusion technique, and found considerably better agreement with Donoho's theory for concentrations up to 0.2 percent. It is thus likely that the source of the disagreement for the rubies not grown by the vapor phase method is dependent on the crystal growth process. If the Cr ions are not uniformly distributed, then cross-relaxation between exchange-coupled pairs or clusters is a possibility. Crystal imperfections and other magnetic impurities (e.g., Fe^{3+}) could similarly affect the relaxation behavior of the Cr ions. Standley and Vaughan [5] discuss these possibilities further. To account for these effects, Donoho's theory would most likely have to be modified to include spin-spin interactions. Previous attempts to incorporate spin-spin effects have not been very successful [30].

Professor Sheldon Shultz at the University of California, San Diego is presently under contract with JPL to perform T_1 measurements at 9 GHz and 35 GHz on our Czochralski-grown ruby. These measurements are being made to determine the optimum Cr concentration in a 32-GHz traveling wave maser (TWM) as a function of temperature, and also to better understand the relaxation mechanism in ruby. Previous measurements [2] have indicated a strong dependence of inversion ratio and gain on Cr concentration, particularly at very low temperatures (e.g., ~ 2 K). This effect is a result of spin-spin interactions, and cannot be explained by Donoho's theory.

V. Calculation of Gain, Pump Power, and Noise Temperature for Ruby

Gain, pump power requirements, and noise temperature are important considerations in maser design and operation. In principle, each of these quantities can be predicted given an accurate knowledge of the spin-lattice transition probability rates, ω_{ij}.

A. Inversion Ratio

The gain in the ruby is directly proportional to the population difference of the inverted levels. The steady-state populations of the levels can be determined as a function of pump power from the steady-state rate equations:

$$\dot{n}_i = 0 = \sum_{j=1}^{4} \left[\omega_{ji} n_j - \omega_{ij} n_i + W_{ij} \left(n_j - n_i \right) \right]$$

$$i = 1, 2, 3, 4 \qquad (51)$$

where W_{ij} is the stimulated transition rate due to RF pumping given by Eq. (5). Applying conservation of spins, Eq. (51) may be reduced to a set of three equations,

$$A' \bar{n} = \bar{b} \qquad (52)$$

where $\bar{n}$ is given by Eq. (40),

$$\bar{b} = -N \begin{bmatrix} \omega_{41} \\ \omega_{42} + W_{24} \\ \omega_{43} + W_{34} \end{bmatrix} \qquad (53)$$

and

$$A' = A + \begin{bmatrix} -(W_{12} + W_{13}) & W_{12} & W_{13} \\ (W_{12} - W_{24}) & -(W_{12} + 2W_{24}) & -W_{24} \\ (W_{13} - W_{34}) & -W_{34} & -(W_{13} + 2W_{34}) \end{bmatrix} \qquad (54)$$

where A is given by Eq. (42). The population vector $\bar{n}$ is determined by matrix inversion. Note that the W_{ij} terms present in $\bar{b}$ and A' are restricted to W_{13}, W_{24}, W_{12}, and W_{34}, corresponding to the transitions that would be pumped in the double pumping schemes shown in Fig. 3. (The choice of these pumping schemes is discussed in [9].)

It is assumed that the signal transition is far from saturation, so W_{signal} can be neglected compared to W_{pump} and ω_{ij}. (Actually, W_{signal} could be $> \omega_{ij}$ for some transitions, but it is assumed this has negligible effect on the populations.)

A convenient measure of the inverted population difference is the inversion ratio, defined for the signal transition occurring between levels i and $j (i > j)$ as

$$I = \frac{n_i - n_j}{N_j - N_i} \qquad (55)$$

where n_i and n_j are determined from Eq. (52). Plots of I versus W_{pump} may be made with temperature, frequency, angle, etc. as parameters.

Figure 4 shows I versus W_{pump} for $f = 32$ GHz, $\theta = 54.7$ deg, and for a range of temperatures. Figure 5 is a similar family of curves for $\theta = 90$ deg. Note the opposite dependence of I on temperature for the two pumping schemes when the pumping rates are near saturation. This is a result of the settling of spins into the lowest energy state as hf/kT increases.

The inversion ratio corresponding to saturation of the pumped transitions can easily be read off of plots of I versus W_{pump}. However, if pump saturation is expected, then the saturation inversion ratio can be determined directly from a single steady-state rate equation. A simple algebraic equation then results for I.

Figure 6 shows I versus temperature assuming pump saturation for the 8.5-GHz maser pumping scheme [1]. Siegman [2] defines the "optimum" and "equal" inversion ratios by rewriting the expression for I in terms of a pseudo-relaxation time,

$$T_{ij} = (\omega_{ij} + \omega_{ji})^{-1} \tag{56}$$

and then either optimizing I with respect to the T_{ij}, or simply setting all the T_{ij} equal and calculating the resulting I. (Siegman does not discuss the theory of spin-lattice relaxation quantitatively, and therefore has to make assumptions about the ω_{ij}.) Note that in Fig. 6 the inversion ratio for saturation is close to the optimum value possible for this pumping scheme. Figure 6 will be compared with measurements being performed at JPL.

Figures 7 and 8 show predicted values I versus temperature for two pumping schemes for a 32-GHz maser. Note that the assumption of pump saturation may not be correct for the higher pump frequencies.

Many measurements of inversion ratio have been performed by R. Clauss et al. [25, 26] at JPL. Table 2 compares some of these measured values with predictions from the spin-lattice relaxation theory. In most cases, it can be assumed that the pump transitions were saturated. The agreement between measurement and theory is moderate, with predicted values often being 30 percent or more different from the measured values.

Inversion ratio measurements have also been performed by Moore and Neff [27] at $\theta = 54.7$ deg. Their results are shown in Fig. 9 with the theoretical value overlayed. The agreement between specific values varies, but the trend of decreasing inversion ratio with increasing signal frequency is predicted by the theory. Note the large scatter in Moore and Neff's measured values of I at frequencies below 20 GHz.

The source of disagreement between the measured and predicted values of I is most likely due to spin-spin interactions, as discussed in Section IV.

B. Gain of Ruby

Expressions for maser gain are given in [2]. Considering only first-order temperature-dependent terms, the gain in dB is

$$G_{\text{dB}} \propto \Delta n_{\text{signal}} \cdot \sigma^2_{\text{signal}} \tag{57}$$

where $\Delta n_{\text{signal}} = I \Delta N_{\text{signal}}$ and where ΔN_{signal} is determined from the Boltzmann relations. Figure 10 shows G_{dB} (normalized to G_{dB} at 4.2 K) versus temperature for the JPL X-band maser pumping scheme. Since $hf/kT \ll 1$ (approximately) even at $T = 1.5$ K, little departure from the expected T^{-1} behavior (dashed line) is seen [2].

For $f = 32$ GHz, $hf/kT \approx 1$ for $T = 1.5$ K, so some deviation of G_{dB} from a T^{-1} dependence is expected. Figure 11 shows the thermal equilibrium population difference (normalized to the population difference at 4.2 K) for the maser configurations shown in Figs. 3(a) and 3(b). Note the strong departure from the T^{-1} curve for the pumping schemes employing the 2-3 signal transition. However, the temperature dependence of G_{dB} is proportional to $I \cdot \Delta N$. Figure 7 displays an inversion ratio that increases as T decreases, so the product $I \cdot \Delta N$ will not deviate greatly from a T^{-1} dependence.

Figure 12 shows normalized gain as a function of temperature for the two pumping scenarios corresponding to Figs. 7 and 8. Both curves are normalized to the gain at 4.2 K for the scenario employing the 2-3 signal transition, and both assume pump saturation. The plots indicate that the 90-deg scheme (1-2 signal transition) will yield greater ruby gain for all temperatures in the range of 1.5 K to 4.2 K.

C. Pump Power

After the pump transition rate W_{ij} is determined for a given inversion ratio, the corresponding pump power can be calculated from W_{ij}. To simplify the expression for W_{ij} as given by Eq. (5), Siegman [2] defines the vector

$$\overline{\sigma}_{ij} = \left\langle \Psi_i \middle| \overline{S} \middle| \Psi_j \right\rangle \tag{58}$$

where $\overline{\sigma}_{ij}$ is a measure of the strength of the i, j transition. Equation (5) then becomes

$$W_{ij} = \frac{1}{4}\gamma^2 g(f) \left| \overline{H}_1^* \cdot \overline{\sigma}_{ij} \right|^2 \tag{59}$$

The maximum value of σ_{ij}^2 occurs when $\overline{H}_1$ and $\overline{S}$ are parallel. Siegman further defines

$$\overline{\sigma}_{ij} = \frac{1}{2}\left(\alpha_{ij}\hat{x} + \sqrt{-1}\,\beta_{ij}\hat{y} + \gamma_{ij}\hat{z}\right) \tag{60}$$

The vector components α_{ij}, β_{ij}, γ_{ij} are determined from the spin Hamiltonian. The optimum polarization of $\overline{H}_1$ is then easily found by maximizing $\overline{H}_1^* \cdot \overline{\sigma}_{ij}$.

Rather than outlining a general procedure for calculating pump power, a specific calculation for a single channel of the 32-GHz reflected wave maser (RWM) [28] is given. The RWM consists of 8 channels of ruby-filled waveguide in which both the signal and pump power propagate in the TE_{10} mode. (Note that at the pump frequency the waveguide can support higher-order modes; here it is assumed that none of these is excited.)

The geometry of a single waveguide channel is shown in Fig. 13. Note that the z axis is defined to be parallel to the dc field $\overline{B}$, unlike Fig. 1 in which the z axis is parallel to the crystal c axis. Thus, the $\overline{\sigma}_{ij}$ vectors computed from the spin Hamiltonian given by Eq. (1) must be rotated through an angle $\theta = 54.7$ deg to apply to Fig. 13.

The RWM employs the push-pull pumping scheme (Fig. 3b) at the double-pump angle $\theta = 54.7$ deg. The pump transitions are the 1-3 and 2-4 at 66 GHz, and the signal transition is the 2-3 at 32 GHz. The $\overline{\sigma}_{ij}$ components are the following:

$$\begin{array}{lll} \alpha_{13} = -0.291 & \beta_{13} = 0.303 & \gamma_{13} = -0.198 \\ \alpha_{24} = -0.257 & \beta_{24} = 0.236 & \gamma_{24} = -0.198 \\ \alpha_{23} = -1.96 & \beta_{23} = 1.96 & \gamma_{23} = 0.085 \end{array} \tag{61}$$

Concentrating on the 1-3 pump transition, note that

$$\overline{\sigma}_{13} \approx \frac{\alpha_{13}}{2}\left(-\hat{x} + j\hat{y} - \frac{2}{3}\hat{z}\right) \tag{62}$$

where $\alpha_{13} \approx 0.30$.

The magnetic field of the TE_{10} rectangular waveguide mode is [29]

$$\overline{H}_1 = \frac{E_0}{Z_d}\left(j\frac{\lambda_d}{2a}\cos\frac{\pi y}{a}\hat{x} + \sqrt{1-\left(\frac{\lambda_d}{2a}\right)^2}\sin\frac{\pi y}{a}\hat{y}\right) \times e^{j(\beta x+\omega t)} \tag{63}$$

where E_0 is the electric-field amplitude, $Z_d = \sqrt{\mu_0/\epsilon}$ is the dielectric impedance, $\lambda_d = \lambda_{\mathrm{freespace}}/\sqrt{\epsilon_r}$ is the dielectric wavelength, and β is the mode propagation constant. For ruby $\epsilon_r \approx 10$, so $Z_d \approx 120\Omega$ and $\lambda_d \approx 0.0566$ in. The RWM guide dimensions are $a = 0.10$ in. and $b = 0.05$ in. [28]. From Eq. (63), $\overline{H}_1$ is circularly polarized for

$$\tan\frac{\pi y}{a} = \frac{\frac{\lambda_d}{2a}}{\sqrt{1-\left(\frac{\lambda_d}{2a}\right)^2}} \tag{64}$$

which has the solutions $y \approx 0.1a$ and $y \approx 0.9a$. Forming the product $\overline{H}_1{}^* \cdot \overline{\sigma}_{13}$, it is found that the pump RF field is most strongly coupled to the spins at $y \approx 0.1a$.

Neglecting losses and ruby absorption, the time-average power flow down the waveguide is [29]

$$P_{\mathrm{avg}} = \frac{Z_{\mathrm{TE}}}{2}\int_{\substack{\text{cross}\\\text{section}}} |H_t|^2\, dA \tag{65}$$

where H_t is the transverse component of H_1 and

$$Z_{\mathrm{TE}} = \frac{Z_d}{\sqrt{1-\left(\frac{\lambda_d}{2a}\right)^2}} \tag{66}$$

Evaluating Eq. (65) and solving for E_0, one obtains

$$E_0 = \left(\frac{4 \cdot P_{\mathrm{avg}} \cdot Z_{\mathrm{TE}}}{a \cdot b}\right)^{1/2} \tag{67}$$

Assuming $P_{\text{avg}} = 50$ mW per channel [28], an electric-field amplitude $E_0 = 2.78 \times 10^3$ V/m is obtained in the guide.

Substituting Eq. (62) into Eq. (59) and noting that H_1 has no z component,

$$W_{13} = \frac{1}{16}\alpha_{13}^2\gamma^2 g(f) \left| \overline{H}_1^* \cdot (\hat{x} - j\hat{y}) \right|^2 \tag{68}$$

Since $\overline{H}_1$ varies as a function of y, an average value of the modulus-squared quantity in Eq. (68) is required. Evaluating the average, one obtains

$$\frac{1}{a}\int_0^a \left| \overline{H}_1^* \cdot (\hat{x} - j\hat{y}) \right|^2 dy = \frac{1}{2}\left(\frac{E_0}{Z_d}\right)^2 \tag{69}$$

Equation (68) averaged over the waveguide cross section becomes

$$\left\langle W_{13} \right\rangle_{\text{c.s.}} = \frac{1}{32}\alpha_{13}^2\gamma^2 g(f) \left(\frac{E_0}{Z_d}\right)^2 \tag{70}$$

To evaluate Eq. (70), one needs to know the line shape function $g(f)$. For an unbroadened Lorentzian line of width Δf_L, the line shape at the pump frequency is [2]

$$g(f_p) \approx \frac{2}{\pi \Delta f_L} \tag{71}$$

where $\Delta f_L \approx 60$ MHz for ruby.

For a line broadened by a stagger-tuned dc field and assuming that the pump sweep rate $\gg$ the pump level relaxation time, the line shape is approximately [2]

$$g(f) = \begin{cases} \dfrac{1}{\frac{\partial f_p}{\partial f_s}\Delta f_s} & f_p - \frac{\Delta f_p}{2} < f < f_p + \frac{\Delta f_p}{2} \\ 0 & \text{elsewhere} \end{cases} \tag{72}$$

where Δf_p and Δf_s are the pump and signal linewidths, and $\partial f_p / \partial f_s$ is evaluated by differencing or by application of the Hellman-Feynman theorem [7]. For the 32-GHz pumping scheme used in the RWM, $\partial f_p / \partial f_s \approx 2$. A typical broadened linewidth for the RWM is $\Delta f_s = 400$ MHz.

Evaluating Eq. (70) for the above values, and noting that $\gamma = 2.2 \times 10^5$ m/Coulomb,

$$W_{13} \approx \begin{cases} 780 \text{ sec}^{-1} & \text{unbroadened} \\ 90 \text{ sec}^{-1} & \text{broadened} \end{cases} \tag{73}$$

From Fig. 4, the corresponding inversion ratios at $T = 4.5$ K are

$$I \approx \begin{cases} 1.3 & \text{unbroadened} \\ 0.8 & \text{broadened} \end{cases} \tag{74}$$

These values compare favorably with the corresponding experimental values. Moore and Neff [27] found the maximum inversion ratio to be $I = 1.1$ to 1.2. (The saturation value of I in Fig. 4 is $I \approx 1.5$). Shell and Neff [28] determined the inversion ratio of the RWM broadened to 400 MHz to be $I \approx 0.7$ to 0.8.

D. Noise Temperature

Amplifier noise temperature T_a' is plotted versus physical temperature T with the resistive loss quantity β as a parameter for the two 32-GHz pumping schemes shown in Figs. 7 and 8. Following Stelzreid [12], the amplifier noise power is

$$P_{\text{n,amp}} = G\, kT_a'\, B \tag{75}$$

where G is the amplifier gain and B is the bandwidth. To make this definition valid for $hf/kT_a' \gtrsim 1$, define

$$T_a' = \frac{\frac{hf}{k}}{e^{\frac{hf}{kT_a}} - 1} \tag{76}$$

where T_a is defined by the black-body noise power

$$P_{\text{n,amp}} = G\frac{hfB}{e^{\frac{hf}{kT_a}} - 1} \tag{77}$$

Noise in masers is discussed thoroughly in [2]. The two primary noise mechanisms are spontaneous emission of photons by the ruby spins and conductor losses in the microwave circuitry. The noise power of a TWM is [2]

$$P_{\mathrm{n,amp}} = (G-1)\left(\frac{\alpha_m}{\alpha_0 - \alpha_m} P_n(-T_m) + \frac{\alpha_0}{\alpha_m - \alpha_0} P_n(T)\right) \tag{78}$$

where

$$P_n(T_0) = \frac{hfB}{e^{\frac{hf}{kT_0}} - 1} \tag{79}$$

and

$$G = e^{2(\alpha_m - \alpha_0)L} \tag{80}$$

where α_m and α_0 are the ruby gain and forward loss coefficients, respectively, of the TWM, and L is the structure length. $T_m = |T_s|$ is the magnitude of the spin temperature defined by the ratio of the inverted spin populations:

$$\frac{n_i}{n_j} = e^{-\frac{hf_{ij}}{kT_s}} \quad i > j \tag{81}$$

For $G \gg 1$, Eqs. (75), (78), and (79) yield a noise temperature

$$T_a' = \frac{hf}{k(1-\beta)}\left[\frac{1}{1 - e^{-\frac{hf}{kT_m}}} + \frac{\beta}{e^{\frac{hf}{kT}} - 1}\right] \tag{82}$$

where $\beta = \alpha_0/\alpha_m$. Figures 14 and 15 show T_a' versus T with β as a parameter and assuming pump level saturation. The figures display a slightly lower T_a' at a given physical temperature and β for the 90-deg orientation. The difference arises from the lower T_m for the 90-deg pumping scheme. Note that at $T = 1.5$ K the effect of β is diminished. Estimates of β for a 32-GHz TWM are not available at this time. For the RWM, Shell and Neff [28] estimate $\beta \sim 0.1$.

VI. Conclusions

This article shows that by accounting for the rate of spin relaxation from higher energy levels, predictions of many basic maser parameters such as gain, pump power, and noise temperature can be made. For ruby, the dominant source of spin relaxation is interaction of the Cr^{3+} ions with thermal vibrations of the Al_2O_3 lattice. Based on measurements found in the literature which characterize the strength of the coupling between the spins and the lattice, quantitative estimates of the spin relaxation rates have been made.

Relaxation time measurements are presently underway at 9 GHz and 35 GHz as a check of the theory and to determine the best orientations and Cr concentration of the ruby crystal for a 32-GHz maser. Previous relaxation time measurements have shown varying degrees of agreement with the theory, perhaps due to the presence of impurities or due to clustering of Cr ions. To account for impurities or clustering, the theory would have to be modified to account for spin-spin interactions.

Comparison of predicted inversion ratios with measured values also shows varying degrees of agreement, but the agreement is generally good. More detailed experimental studies of inversion ratio and gain for various levels of pump power and as a function of physical temperature for the 54.7-deg and 90-deg ruby orientations are necessary at 32 GHz.

The theory predicts that at 32 GHz and assuming pump saturation, the gain for the 90-deg orientation (1-2 signal transition) should be nearly 50 percent higher in dB than for the 54.7-deg orientation (2-3 signal transition). The theory also predicts a slightly lower noise temperature for the 90-deg orientation. Although specific calculations have not been performed, it is expected that the 90-deg orientation will require ≈ 50 percent greater pump power than the 54.7-deg orientation.

The usefulness of the present theory remains to be seen. It may be found that spin-spin interactions cannot be neglected even for the relatively dilute ruby used in maser amplifiers. The theory is, however, a significant step towards a more complete understanding of ruby masers.

References

[1] S. Petty, "Introduction to Microwave Devices, Part VIII," in *Low Temperature Electronics*, edited by R. Kirschman, New York: IEEE Press, pp. 358–363, 1986.

[2] A. Siegman, *Microwave Solid-State Masers*, New York: McGraw-Hill, 1964.

[3] R. B. Hemphill, P. L. Donoho, and E. D. McDonald, "Spin-Lattice Interaction in Ruby Measured by Electron Spin Resonance in Uniaxially Stressed Crystals," *Physical Review*, vol. 146, pp. 329–335, 1966.

[4] P. L. Donoho, "Spin Lattice Relaxation in Ruby," *Physical Review*, vol. 133, pp. A1080–A1084, 1964.

[5] K. J. Standley and R. A. Vaughan, *Electron Resonance Phenomena in Solids*, London: Adam Hilger LTD, 1969.

[6] B. Bleaney and W. Stevens, "Paramagnetic Resonance," *Reports Prog. Phys.*, vol. 16, pp. 108–159, 1953.

[7] P. W. Atkins, *Molecular Quantum Mechanics*, 2nd ed., Oxford: Oxford University Press, 1983.

[8] R. Berwin, "Paramagnetic Energy Levels of the Ground State of Cr^{3+} in Al_2O_3 (Ruby)," *Technical Memorandum 33-440*, Jet Propulsion Laboratory, Pasadena, California, January 1970.

[9] J. R. Lyons, "Theoretical Comparison of Maser Materials for a 32-GHz Maser Amplifier," *TDA Progress Report, 42-95*, vol. July–September 1988, Jet Propulsion Laboratory, Pasadena, California, pp. 58–70, November 15, 1988.

[10] E. Schulz-Du Bois, "Paramagnetic Spectra of Substituted Sapphires—Part 1: Ruby," *Bell Syst. Tech. J.*, vol. 38, pp. 271–290, 1959.

[11] L. Schiff, *Quantum Mechanics*, 3rd ed., New York: McGraw-Hill, 1968.

[12] C. T. Stelzreid, *The Deep Space Network—Noise Temperature Concepts, Measurements, and Performance*, JPL Publication 82-33, Jet Propulsion Laboratory, Pasadena, California, 1982.

[13] A. Abragam and B. Bleaney, *Electron Paramagnetic Resonance of Transition Ions*, New York: Dover, 1986.

[14] R. D. Mattuck and M. W. P. Strandberg, "Spin-Phonon Interaction in Paramagnetic Crystals," *Phys. Rev.*, vol. 119, pp. 1204–1217, 1960.

[15] E. B. Tucker, "Interaction of Phonons with Iron-Group Ions," *Proc. of IEEE*, vol. 53, pp. 1547–1573, October 1965.

[16] J. H. Van Vleck, "Paramagnetic Relaxation Times for Titanium and Chrome Alum," *Physical Review*, vol. 57, pp. 426–447, 1940.

[17] F. Fumi, "The Direct-Inspection Method in Systems with a Principal Axis of Symmetry," *Acta Cryst.*, vol. 5, pp. 691–694, 1952.

[18] C. Kittel, *Introduction to Solid State Physics*, 6th ed., New York: John Wiley & Sons, 1986.

[19] I. Manenkov and R. Orbach, *Spin-Lattice Relaxation in Ionic Solids*, New York: Harper and Row, 1966.

[20] *CRC Handbook of Chemistry and Physics*, edited by R. C. Weast, Cleveland: The Chemical Rubber Co., 1970.

[21] H. B. Huntington, "Elastic Constants of Crystals," in *Solid State Physics*, vol. 7, Seitz and Turnbull, eds., New York: Academic Press, 1958.

[22] J. B. Wachtman, Jr., W. E. Tefft, D. G. Lam, Jr., and R. P. Stinchfield, "Elastic Constants of Synthetic Single Crystal Corrindum at Room Temperature," *J. of Res. of N.B.S.*, vol. 64A, pp. 213–228, 1960.

[23] J. N. Franklin, *Matrix Theory*, Englewood Cliffs, New Jersey: Prentice-Hall, 1968.

[24] K. J. Standley and R. A. Vaughan, "Effect of Crystal-Growth Method on Electron Spin Relaxation in Ruby," *Phys. Rev.*, vol. 139, pp. A1275–A1280, 1965.

[25] R. Clauss, "RF Techniques Research: System Studies for Frequencies Above S-Band for Space Communications," *JPL Space Programs Summary 37-61*, vol. III, Jet Propulsion Laboratory, Pasadena, California, pp. 90–93, February 1970.

[26] R. Berwin, R. Clauss, and E. Wiebe, "Low-Noise Receivers: Microwave Maser Development," *JPL Space Programs Summary 37-56*, vol. II, Jet Propulsion Laboratory, Pasadena, California, pp. 101–105, March 1969.

[27] C. Moore and D. Neff, "Experimental Evaluation of a Ruby Maser at 43 GHz," *IEEE Trans. MTT*, vol. 30, pp. 2013–2015, 1982.

[28] J. Shell and D. Neff, "A 32-GHz Reflected-Wave Maser Amplifier with Wide Instantaneous Bandwidth," *TDA Progress Report 42-94*, vol. April–June 1988, Jet Propulsion Laboratory, Pasadena, California, pp. 145–162, August 15, 1988.

[29] S. Ramo, J. Whinnery, and T. Van Duzer, *Fields and Waves in Communication Electronics*, New York: John Wiley & Sons, 1965.

[30] J. Owen and E. A. Harris, "Pair Spectra and Exchange Interaction," Chap. 6, in *Electron Paramagnetic Resonance*, ed. S. Geschwind, Plenum Press, 1972.

Table 1. Comparison of Donoho's [4] calculated values of A_i and T_i with those of the author for $\theta = 54.7$ deg, f = 9.3 GHz, and T = 4.2 K

$\theta = 54.7$ deg, transition = 2-3		
	Donoho's Calculation [4]	Author's Calculation
T_1	0.38	0.20
T_2	0.22	0.11
T_3	0.13	0.07
A_1	0.99	1.00
A_2	0	0
A_3	0	0

$\theta = 54.7$ deg, transition = 3-4		
	Donoho's Calculation [4]	Author's Calculation
T_1	0.97	0.51
T_2	0.60	0.30
T_3	0.22	0.11
A_1	0.50	0.26
A_2	0.41	0.49
A_3	0.09	0.25

Table 2. Comparison of measured inversion ratio with theoretical predictions for 0.05 percent Cr ruby at 4.5 K

θ, deg	H_0, kG	Transition(s) and Frequency, GHz		I^{opt}	I^{meas}	I^{theory}
		Signal	Pump			
54.7	5.72	2-3 14.4	1-3, 2-4 32.9	3.6	2.8[a]	2.2
54.7	5.56	2-3 13.9	1-3, 2-4 32.0	3.6	3.0[a,b]	2.3[b]
54.7	6.78	2-3 17.2	1-3, 2-4 28.0	3.4	3.3	2.0
54.7	3.7	2-3 8.5	1-3, 2-4 21.9	4.2	2.5	3.0
54.7	6.6	2-3 16.8	1-3, 2-4 37.3	3.4	2.5	2.0
90	5.0	1-2 8.5	1-4 43.5	4.1	2.5	3.6
90	5.0	1-2 8.5	1-3, 3-4 24.2, 19.3	4.1	3.2	3.6
90	6.8	1-2 13.6	1-3, 3-4 33.9, 24.6	3.3	3.0	2.7
90	7.1	1-2 14.2	1-3, 3-4 35.2, 25.2	3.2	2.9[b]	2.4[b]
90	8.0	1-2 16.8	1-4 68.3	3.1	−0.1[c]	2.5
90	8.0	1-2 16.8	1-3, 3-4 40.3, 28.0	3.1	2.9	2.4

[a] 0.075 percent Cr

[b] 1.8 K

[c] Pump not saturated

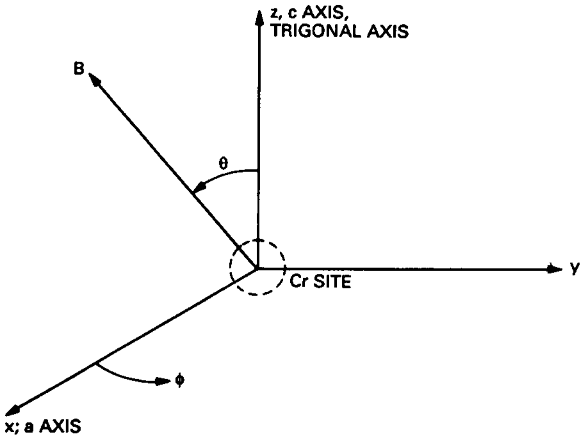

Fig. 1. Geometry of Cr^{3+} site.

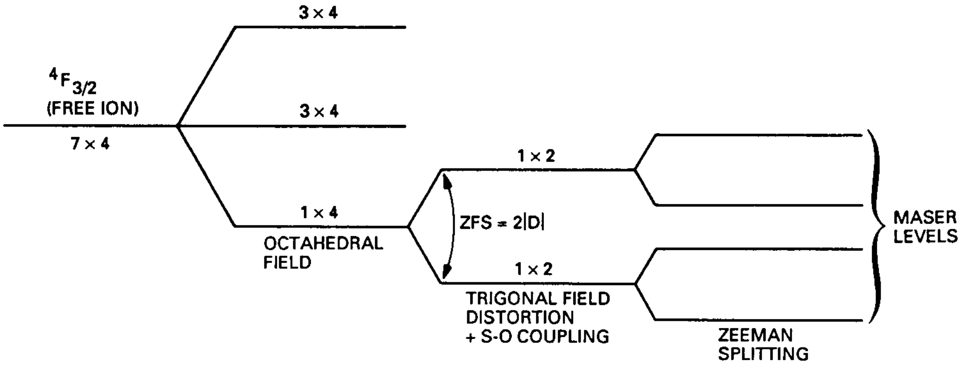

Fig. 2. Simplified energy splitting diagram for Cr in Al_2O_3 lattice. Sequence of quantum mechanical perturbations applied is shown. m × n = m-fold orbital degeneracy and n-fold spin degeneracy.

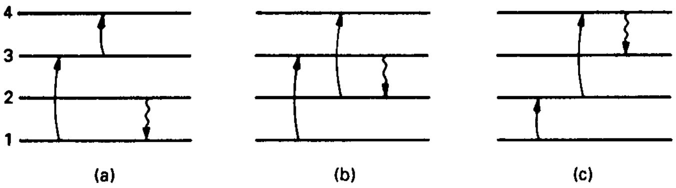

Fig. 3. Double-pumping schemes being considered for ruby for a 32-GHz maser. The downward arrow is the 32-GHz (signal) transition.

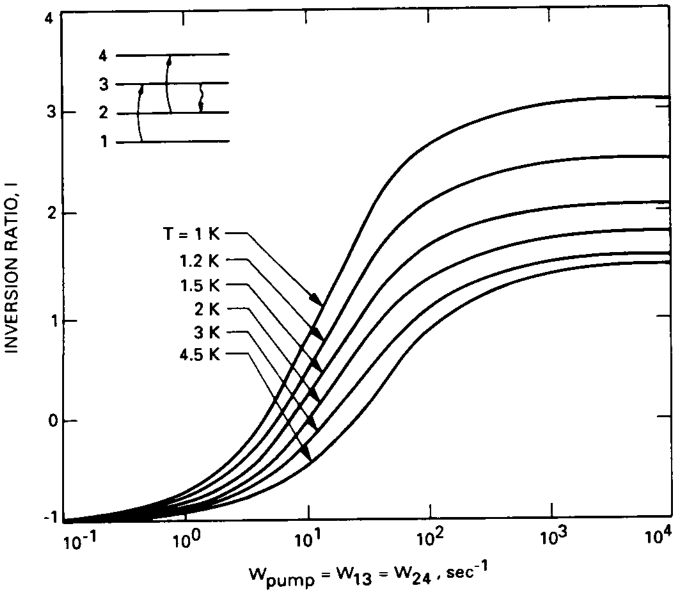

Fig. 4. I versus W_{pump} for $\theta = 54.7$ deg, H = 11.8 kG, signal = 2-3 transition = 32 GHz.

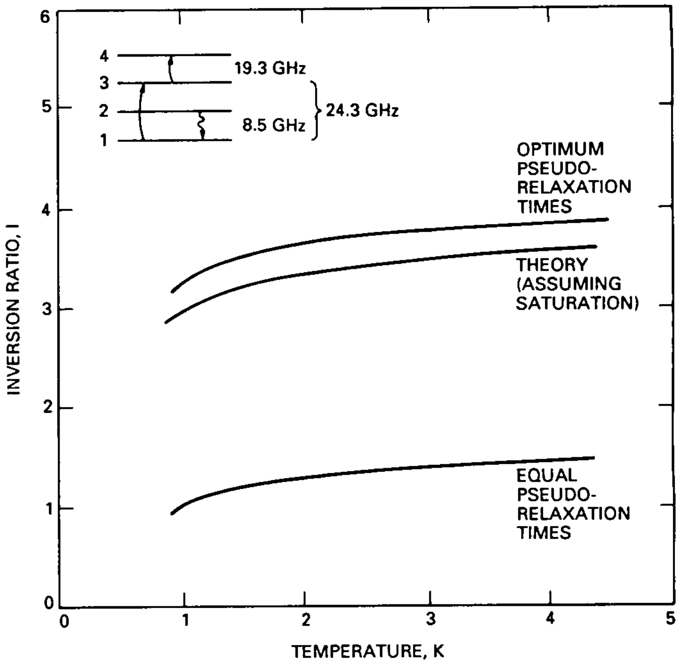

Fig. 6. I versus T assuming saturation for $\theta = 90$ deg, H = 5 kG, signal = 1-2 transition = 8.5 GHz.

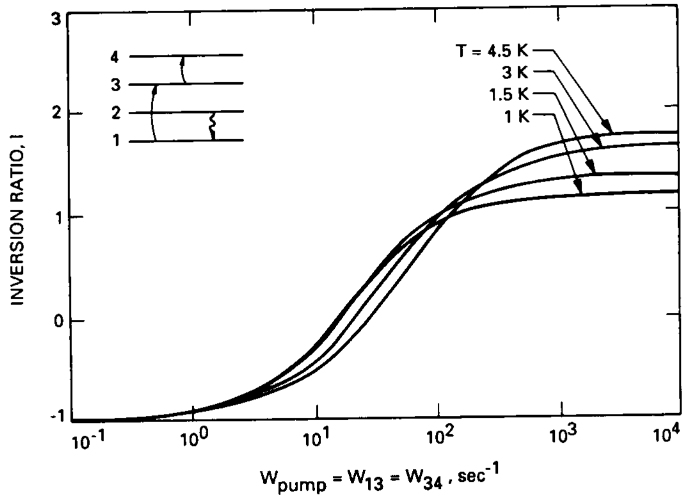

Fig. 5. I versus W_{pump} for $\theta = 90$ deg, H = 13.5 kG, signal = 1-2 transition = 32 GHz.

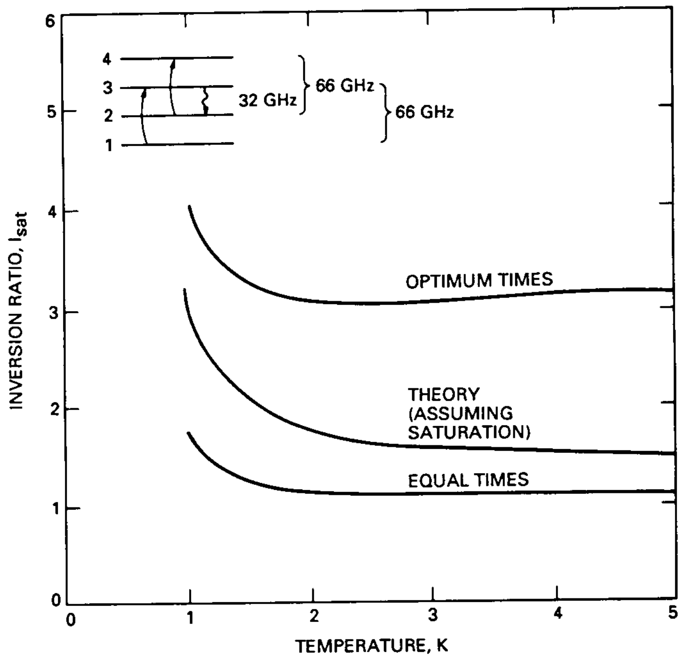

Fig. 7. I versus T assuming saturation for $\theta = 54.7$ deg, H = 11.8 kG, signal = 2-3 transition = 32 GHz.

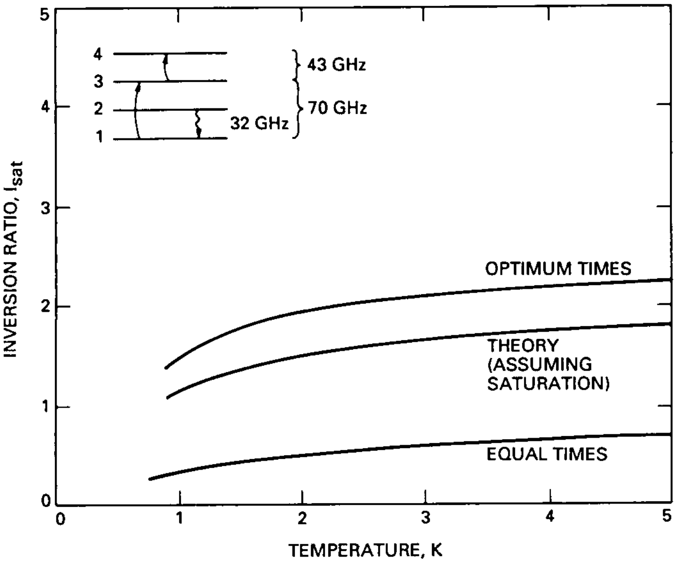

Fig. 8. I versus T assuming saturation for $\theta = 90$ deg, H = 13.5 kG, signal = 1-2 transition = 32 GHz.

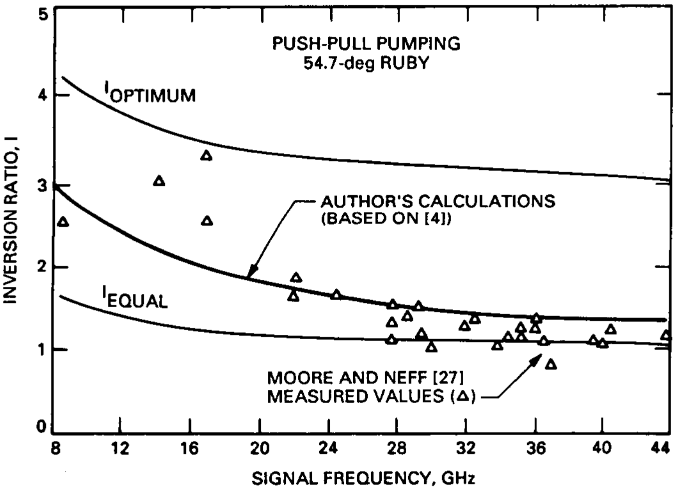

Fig. 9. Measured and theoretical values of I versus signal frequency for ruby, $\theta = 54.7$ deg, T = 4.5 K.

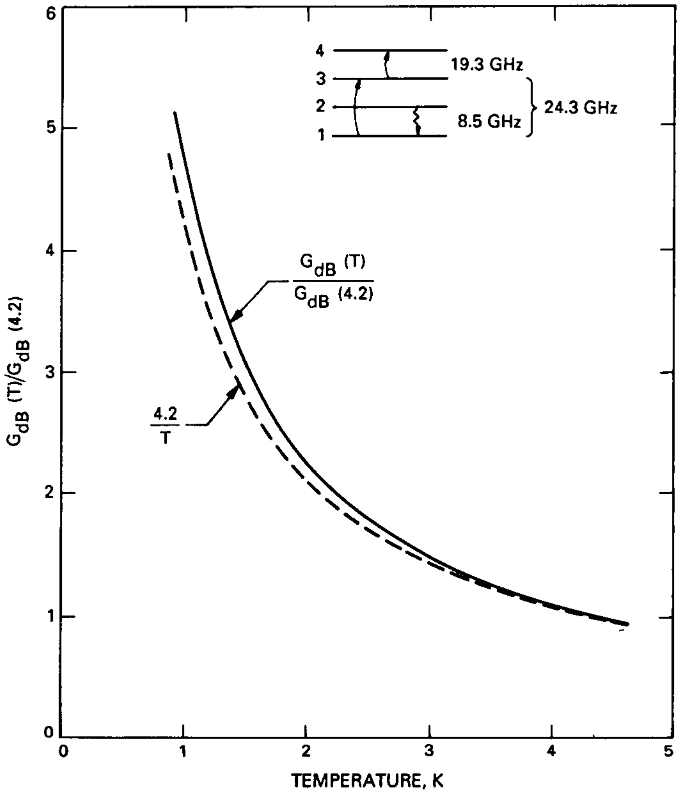

Fig. 10. The normalized gain versus T (assuming saturation) for $\theta = 90$ deg, H = 5 kG, and signal = 1-2 transition = 8.5 GHz.

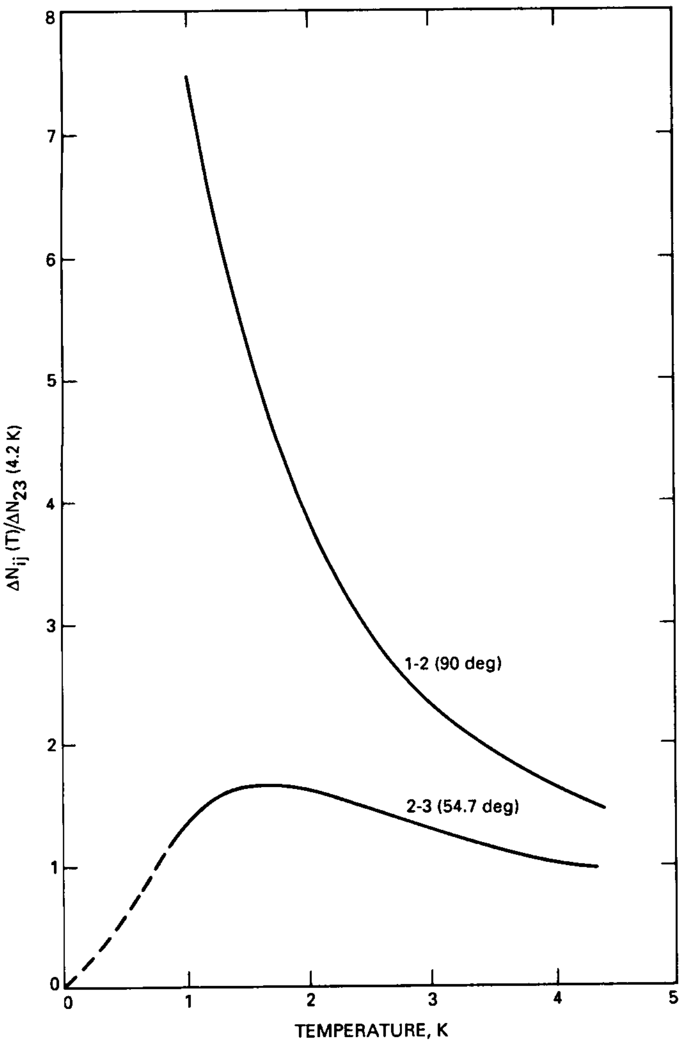

Fig. 11. Thermal equilibrium population difference for two 32-GHz pumping scenarios (normalized to population difference of the 54.7-deg scenario at 4.2 K).

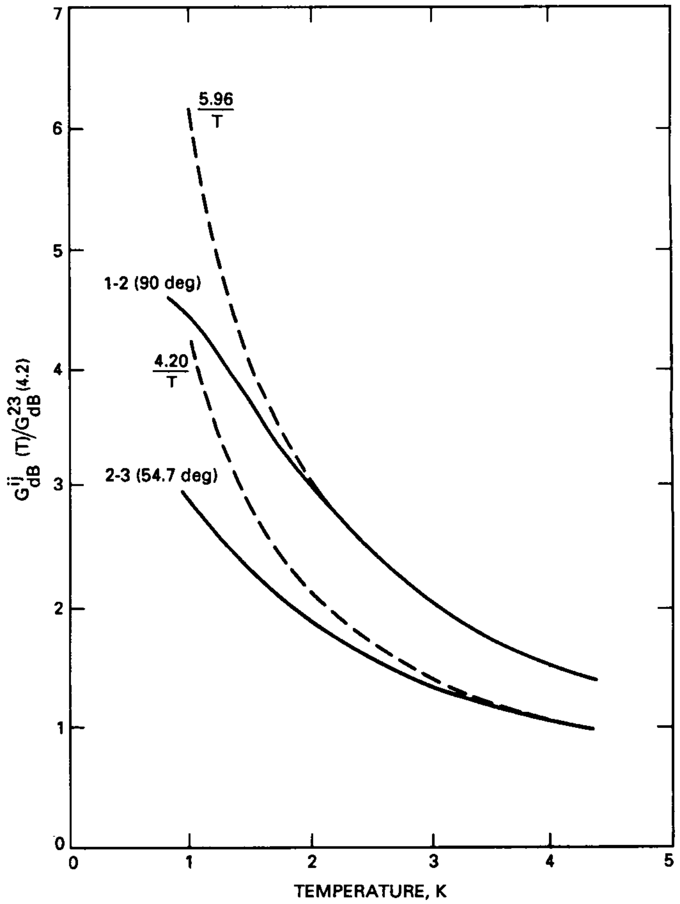

Fig. 12. G_{dB} versus T for 54.7-deg and 90-deg pumping schemes (assuming saturation).

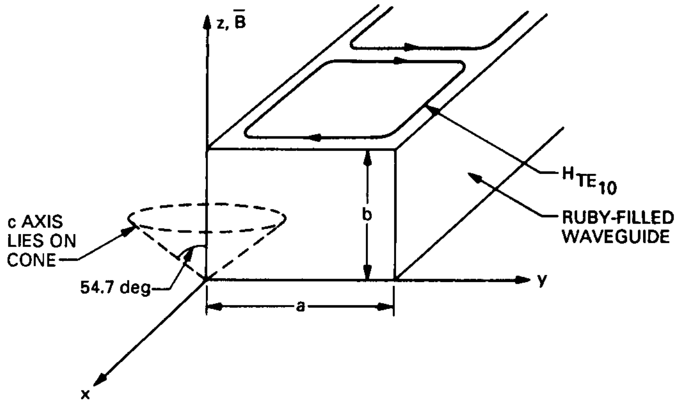

Fig. 13. Geometry of a single channel of ruby-filled waveguide for 32-GHz RWM.

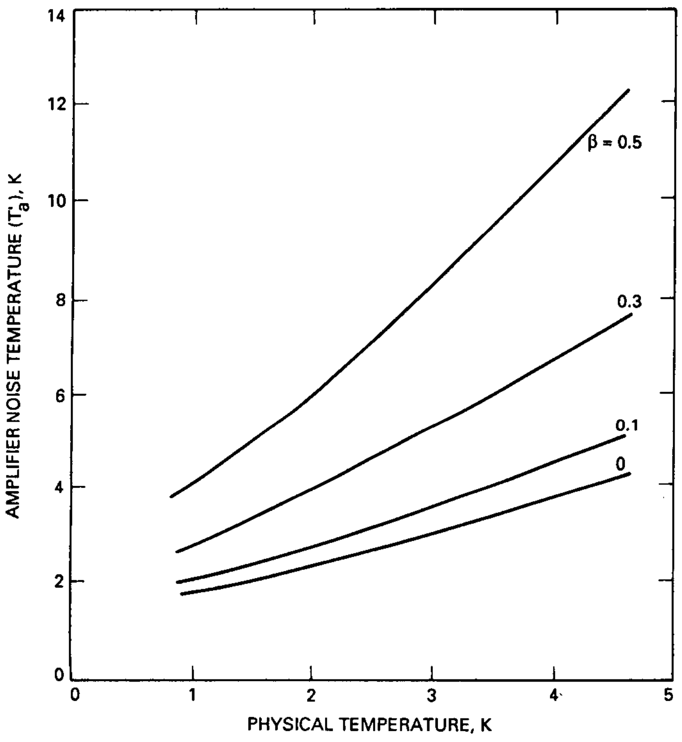

Fig. 14. T'_a versus temperature for 32-GHz ruby maser, $\theta = 54.735$ deg, signal = 2-3 transition = 32 GHz.

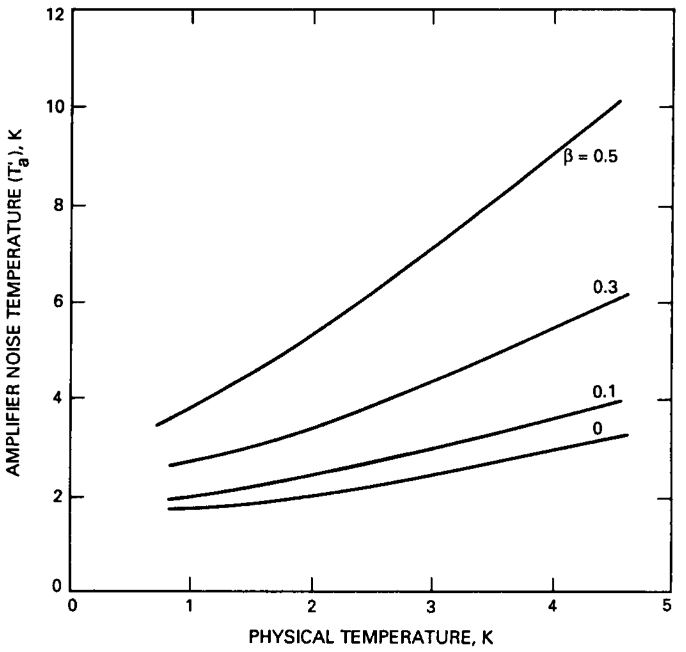

Fig. 15. T'_a versus temperature for 32-GHz ruby maser, $\theta = 90$ deg, signal = 1-2 transition = 32 GHz.